International Journal of Heat and Mass Transfer 51 (2008) 5633–5641

Contents lists available at ScienceDirect

International Journal of Heat and Mass Transfer

journal homepage: www.elsevier.com/locate/ijhmt

Unsteady, three-dimensional fluid mechanic analysis of blood flow in plaque-narrowed and plaque-freed arteries

J.P. Abraham [a,*], E.M. Sparrow [b], R.D. Lovik [b]

[a] Laboratory for Heat Transfer Practice, Department of Engineering, University of St. Thomas, St. Paul, MN, USA
[b] Laboratory for Heat Transfer Practice, Mechanical Engineering Department, University of Minnesota, Minneapolis, MN, USA

ARTICLE INFO

Article history:
Received 3 January 2008
Received in revised form 4 April 2008
Available online 10 June 2008

ABSTRACT

Fluid mechanic analysis is used to create and implement a metric to quantify the effectiveness of plaque removal (i.e., debulking) modalities in small arteries. The quantification is based on a three-dimensional, unsteady model of blood flow in complex tubular geometries which characterizes plaque-narrowed arteries. Blood flow unsteadiness is due to the heart-imposed temporal variations which occur during the cardiac cycle. The arterial geometries used for the analysis were determined by the reconstruction of ultrasonic images which were captured before and after debulking. Numerical simulation was used to implement the fluid mechanic model, and separate consideration is given to Newtonian and non-Newtonian constitutive equations. The results of the analysis indicates that the removal of the plaque led to an increase in the rate of blood flow of approximately 2.5, both during the systole and diastole portions of the cardiac cycle. This increase corresponds to the application of the same time-varying, end-to-end pressure difference across the artery segments. The shear stress on the artery wall, a major determinant of the buildup of plaque, is found to be higher for a debulked artery than for a plaque-narrowed artery. This outcome is favorable in that the higher the wall shear, the lower the rate of plaque formation.

1. Introduction

Fluid mechanic phenomena play a major role in the functioning of virtually all processes that occur in the human body. Most evident among these phenomena is the delivery of oxygen and nutrients to the cells by blood flow and the extraction and transport of wastes by the blood. There is an extensive literature on blood flow in the human body, for instance, Ku [14] and Taylor et al. [27]. The work that is reflected by these references encompasses a wide range of fluid flow models, including steady flow in circular passages in Neofytou and Drikakis [20], O'Callaghan et al. [21], LaDisa et al. [15], Grigoni et al. [10], and Abraham et al. [1]; steady flow in non-circular passages obtained by reconstitution of medical images by Ding et al. [7], Berthier et al. [3], and Shahcheraghi et al. [24]; unsteady flows driven by the pressure waveforms due to the beating heart by Oshima et al. [22], Long et al. [16], Kruger et al. [13], Shahcheraghi et al. [24], Marques et al. [18], Marshall et al. [19], and Chen and Lu [5]; and Newtonian and non-Newtonian constitutive models by Gijsen et al. [9], Cho and Kensey [6], Neofytou and Drikakis [20], and Johnston et al. [12]. Issues such as fluid-structural interactions, specifically the interactions between the blood flow and arterial walls, are only recently being considered by Tang et al. [25,26].

The objective of the present work is somewhat different from that of the aforementioned citations. Here, it is proposed to use fluid mechanic modeling to evaluate the efficacy of a critical therapeutic procedure. Atherosclerosis is a common human affliction in which blood vessels become narrowed and even blocked by the accumulation of plaque deposits on internal surfaces. Among the techniques for removal of the plaque formations, the use of mechanical means has found significant application. These means may include: cutting, sanding, and scraping. Typically, these methods remain unevaluated with regard to outcome and, at best, the evaluation of outcomes is highly qualitative.

The proposal set forth here is to model the blood flow through a plaque-narrowed artery and its counterpart subsequent to removal of plaque by mechanical means. The specific device used here to remove the arterial plaque (to *debulk*) is the Diamondback 360 Orbital Atherectomy System (Cardiovascular Systems Inc., St. Paul, MN). The outcome of the application of this device will be conveyed via reconstituted ultrasound images. Those images, when translated into a solid-model format, create realistic geometries for the application of the fluid mechanic model.

The model will account for the pulsations created by the cardiac cycle and of the complex geometries of both the pre-treated and post-treated artery. The specific artery in question is the posterior tibial, which is situated in the lower leg. This artery is one of the most susceptible to plaque formation.

The specific results that are sought as the outcomes of the modeling effort are the comparative blood flows in the pre-debulked

* Corresponding author. Tel.: +1 651 962 5766; fax: +1 651 962 6419.
E-mail address: jpabraham@stthomas.edu (J.P. Abraham).

0017-9310/$ - see front matter © 2008 Elsevier Ltd. All rights reserved.
doi:10.1016/j.ijheatmasstransfer.2008.04.038

and debulked arteries when subjected to the same time-dependent driving pressures. Of equal relevance as an outcome to the therapeutic procedure is the shear stress exerted by the pulsating flow on the artery walls. These shear stresses play a major role in the recurrence of the plaque (*restenosis*).

2. Creation of the geometrical model

The preliminary work that was necessary for the implementation of this research was the collection of geometric data for the pre-debulked and debulked arteries. The data were collected in an appropriate clinical setting (Integra Solutions, Brooklyn Park, MN) by making use of a previously frozen cadaver. Prior to the debulking procedure, a precisely timed longitudinal transverse was carried out with an ultrasound probe in order to determine the geometry of the artery and its plaque content. The longitudinal traverse produced 300 images, each image being a slice of thickness 0.1 mm. Subsequently, a surgical procedure was performed at the upper thigh to enable introduction of the Diamondback debulking device. The position of the device was achieved by angiographic imaging. Once properly positioned, the device was periodically traversed through the plaqued artery in a longitudinal manner during a 90-s interval. A photograph of the exposed artery is shown in Fig. 1. A 30-mm length of the just-debulked artery was selected to provide the geometry for comparison with that of the pre-debulked artery. Care was taken to use the same 30-mm sample for the pre-debulked and debulked artery evaluation.

The photographs in Fig. 1 show a wide view of the cadaver leg displaying the opened region and the exposed artery system of the lower leg. A callout shows a closeup view of the targeted artery which was treated by the debulking process. The artery has been cut open to show that the inner wall is free of plaque, after the debulking process.

Ultrasonic evaluation of both the pre and post configurations was made. An illustrative set of images of a cross-section of the artery showing features of the two states is presented in Fig. 2. The figure shows the lumen boundary before and after the debulking process. A comparison of the boundary clearly shows an increased lumen diameter as a result of the procedure.

The reconstitution of the geometric images was accomplished by use of Amira 4.1 and Maya 7.0 software programs. To facilitate the use of these programs, the boundary of each slice was smoothed by a splining technique. The outcome of this process were solid-model files with highly precise geometric detail, as shown in Fig. 3. These solid-model files were then employed as input to information to the numerical simulation that will now be described.

3. Mathematical model

The geometries of the fluid flow passages corresponding to the pre-debulked and post-debulked arteries have now been determined. Attention will now be turned to the analysis of the three-dimensional, unsteady flow in these highly irregular tubes. For the analysis, the flow will be regarded as incompressible and the fluid properties to be constant. Two constitutive equations will be employed in the simulation. One is laminar, Newtonian flow, and the other is laminar, non-Newtonian flow. The equations governing the flow are, first, conservation of mass, and second, momentum conservation. Mass conservation is expressed as

$$\frac{\partial u}{\partial x}+\frac{\partial v}{\partial y}+\frac{\partial w}{\partial z}=0 \tag{3.1}$$

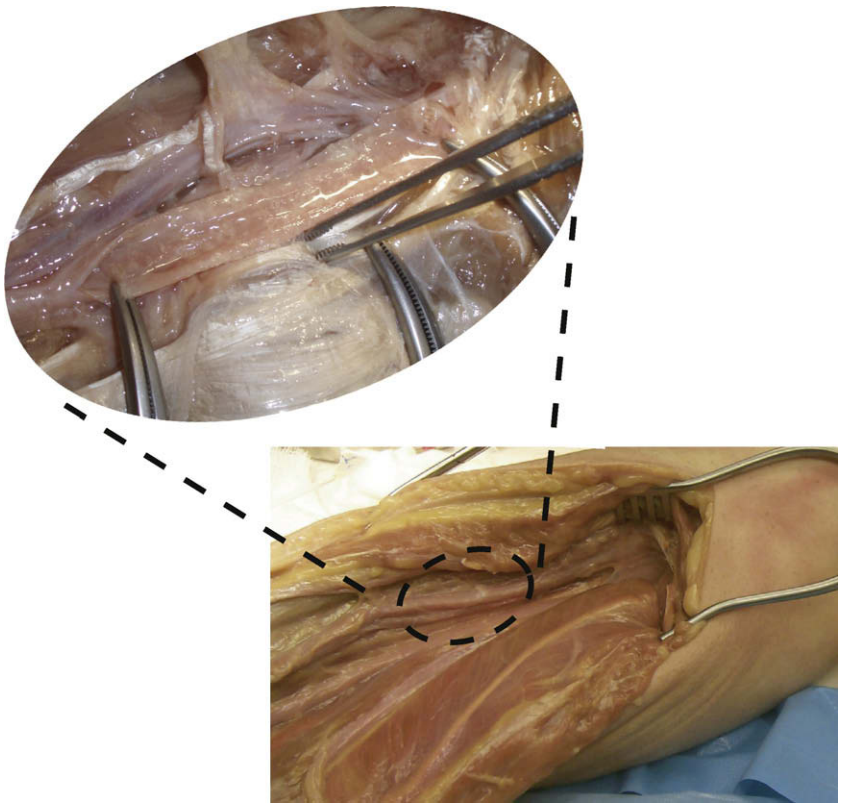

Fig. 1. Photograph showing cadaver with exposed posterior tibial artery. Callout shows closeup view of posterior tibial artery after debulking. Excised artery shows the absence of arterial plaque.

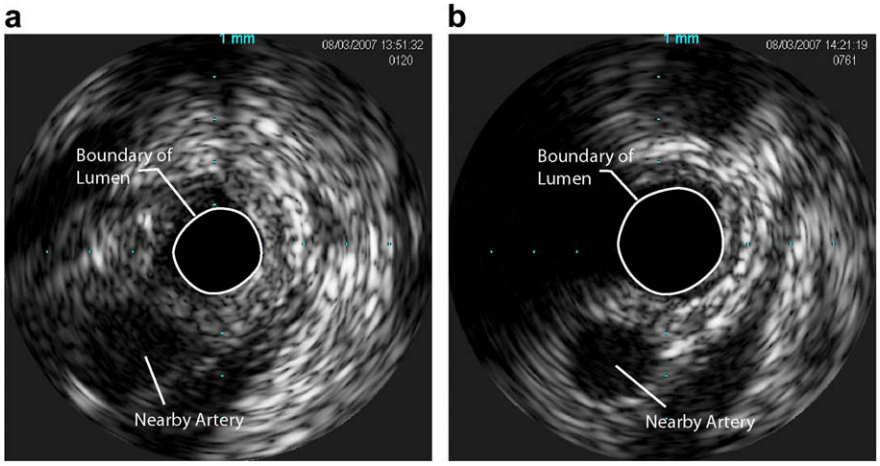

Fig. 2. Intravenous ultrasound images of the cross-section of a posterior tibial artery before (a) and after (b) debulking.

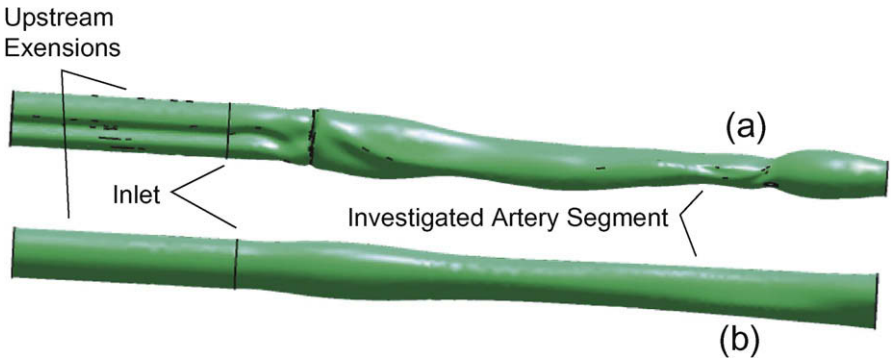

Fig. 3. Reconstituted geometries of the bounding walls of the lumen before (a) and after (b) debulking of the artery.

In this equation, the cross-sectional coordinates are x and y while the z is the axial coordinate. The corresponding velocities are u, v, and w.

The three momentum equations that were solved in this analysis are

$$\rho\left(\frac{\partial u}{\partial t}+\frac{\partial}{\partial x}(u^2)+\frac{\partial}{\partial y}(uv)+\frac{\partial}{\partial z}(uw)\right)=-\frac{\partial p}{\partial x}+\frac{\partial \tau_{xx}}{\partial x}+\frac{\partial \tau_{yx}}{\partial y}+\frac{\partial \tau_{zx}}{\partial z} \tag{3.2}$$

$$\rho\left(\frac{\partial v}{\partial t}+\frac{\partial}{\partial x}(uv)+\frac{\partial}{\partial y}(v^2)+\frac{\partial}{\partial z}(vw)\right)=-\frac{\partial p}{\partial y}+\frac{\partial \tau_{xy}}{\partial x}+\frac{\partial \tau_{yy}}{\partial y}+\frac{\partial \tau_{zy}}{\partial z} \tag{3.3}$$

$$\rho\left(\frac{\partial w}{\partial t}+\frac{\partial}{\partial x}(uw)+\frac{\partial}{\partial z}(vw)+\frac{\partial}{\partial z}(w^2)\right)=-\frac{\partial p}{\partial z}+\frac{\partial \tau_{xz}}{\partial x}+\frac{\partial \tau_{yz}}{\partial y}+\frac{\partial \tau_{zz}}{\partial z} \tag{3.4}$$

The shear stresses appearing in these equations were alternatively evaluated by making use of the Newtonian viscosity of blood, $\mu = 0.00345$ kg/m s, reported in [12] or the Ostwald–de Waele non-Newtonian constitutive model described in Bird et al. [4]. The latter model is represented by

$$\tau = K\gamma^n \tag{X}$$

in which $K = 0.0147$ (kg/m-s$^{1.22}$) and $n = 0.78$ [28]. This non-Newtonian model is frequently used in the analysis of blood flow. In a previous study of a physical situation which possesses similarities to that studied here [30], it was found that the end results were independent of the values of K and n within the normally accepted range for blood [28,29].

4. Implementation of the simulation model

4.1. Spatial and temporal boundary conditions

Blood flow is a cyclic process so that it is only necessary to focus on a single cycle to obtain representative results. In order to obtain a realistic reproduction of the physical situation, information about the cyclic velocity in the posterior tibial artery was extracted from

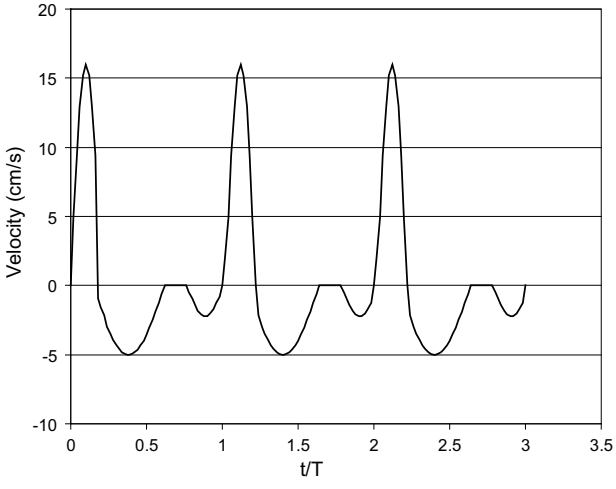

Fig. 4. Velocity waveform applied to debulked artery segment.

Fronek et al. [8]. The cited cross-sectional-average velocity information is reproduced in Fig. 4. Note that the period of the cyclic variation is 1 s. The curve shown in that figure is representative of measurements made in 78 individual arteries in a group of subjects, ages 19–32, who were selected for not having angiographically documented arterial disease.

This information was used as input to the simulations of the debulked artery. On the basis of the numerical results extracted from the simulation, the timewise-varying pressure difference between the respective ends of the investigated length of artery was found. This pressure difference was, in turn, applied to the simulation of the pre-debulked artery. The outcome of this procedure was the timewise variation of the flowrates passing through the debulked and undebulked arteries. The comparison between these flowrates constitutes the definitive improvement of vascular health affected by the debulking procedure.

4.2. Details of the numerical method

The calculations were carried out using CFX 11.0, a commercial finite-volume-based CFD program. The continuity and momentum equations are conserved over each element in the mesh, and overall conservation throughout the entire domain is thereby guaranteed. Solutions were carried out for five cardiac cycles with the view of identifying the periodic steady state. In all cases, it was found that the solution attained the periodic steady state after two cycles of calculations. At each time step, a false-transient approach was employed to enable convergence. The number of iterations performed at each time step was governed by the requirement that the residuals of all transported variables were less than 10^{-5}. In each iteration, a multigrid strategy was used in which contiguous elements are clustered into numerous larger elements, as described by Hutchinson and Raithby [11].

The initial time was set at 0.01 s, and subsequent time steps were bounded between 0.001 and 0.1 s. At each moment of time, the time step was chosen so that convergence of the iterative process to the aforementioned criterion is accomplished well within 10 iterations. The transient discretization scheme is second-order backward difference.

Coupling of the velocity–pressure equations was achieved on a non-staggered, collocated grid using the techniques developed by Rhie and Chow [23] and Majumdar [17]. The inclusion of pressure-smoothing terms in the mass conservation equation suppresses oscillations which can occur when both the velocity and pressure are evaluated at coincident locations.

The advection term in the momentum equations was evaluated by using the upwind values of the momentum flux, supplemented with an advection–correction term. The correction term reduces the occurrence of numerical diffusion and is of second-order accuracy. Details of the advection treatment can be found in Barth and Jesperson [2].

The fact that there is both forward flow and back flow during a given cycle required special consideration which is not needed in normal unidirectional fluid flows. In particular, to deal with such flows, the standard inflow and outflow boundary conditions have to be carefully reexamined. The inflow boundary in the CFX software does permit both positive and negative velocity components. On the other hand, the outflow boundary does not permit flow reversal. Therefore, the outflow boundary condition could not be applied at the downstream end of the length of artery investigated. Instead, it was necessary to employ a special condition (*opening*) in which the software calculates the direction of the flow provided that the pressure at the opening is specified. If the flow passes outward through the opening, the applied boundary condition for all the dependent variables is that their streamwise second derivatives are zero.

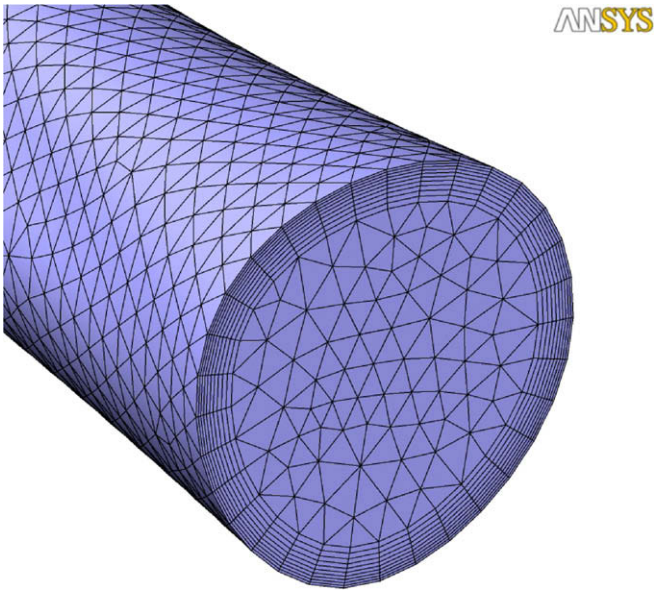

Fig. 5. Display of the computational mesh showing boundary layer elements deployed along the lumen wall.

At the inlet of the investigated artery, the solution domain was extended upstream to investigate the impact of a hydrodynamic starting length. For this purpose, three starting lengths were used, one at the inlet proper, a second at a distance of approximately five diameters upstream of the inlet, and a third approximately ten diameters upstream. When the simulation model results were obtained for the mass flowrate predictions for these three cases, it was found that they could not be visually distinguished from each other. In this light, all subsequent numerical simulations were performed using the model in which the upstream extension of the solution domain was positioned five diameters from the investigated artery segment.

The solution domain was initially discretized by approximately 105,000 elements. A mesh-independence study was subsequently performed with 250,000 elements. The resulting values of the time-integrated mass flowrates from these two meshes agreed to within 1%. The quality of the mesh was tailored by a process called inflation so that the elements could be concentrated in regions of high gradients adjacent to the walls of the artery, as seen in Fig. 5.

5. Results and discussion

5.1. Mass flow and pressure results

The main result of clinical importance is the increase in the rate of blood flow through the debulked artery relative to that carried prior to debulking. These results were obtained by making use of the Ostwald–de Waele non-Newtonian constitutive model. The issue of the impact of the constitutive model will be addressed shortly.

The cycle-integrated results for these quantities are presented in Table 1. The table separately lists the integrated flowrates through the systolic and diastolic periods, both for the pre-debulked and debulked artery configurations. In addition, the increases in these flowrates that result from debulking are highlighted in the rightmost column of the table.

It can be seen that the debulking has a major positive impact on the rate of blood flow. The flowrates after debulking are on the order of 2.5 times those prior to debulking. The clinical importance of this finding is that the lower leg and foot will be strongly perfused

Table 1
Mass flowrates for pre-debulked and debulked artery segments

	Pre-debulked	Debulked	Ratio: Post/Pre
Systole flow (grams/cycle)	0.0353	0.0859	2.43
Diastole flow (grams/cycle)	0.0186	0.0521	2.80
Net flow (grams/cycle)	0.0166	0.0338	2.04

such that the health of the cells in those regions will be significantly enhanced.

As was set forth in the Introduction, one of the major aims of this work is to provide a quantitative metric for the assessment of the efficacy of various debulking modalities. It can be seen from Table 1 that the modality evaluated here can be regarded as being very highly effective in carrying out the mission of improving blood flow by debulking.

A more detailed assessment of the effect of debulking on the mass flowrates can be obtained by examining how the instantaneous flowrates vary during the course of a cycle. This information is displayed in Fig. 6. That figure not only compares the flowrates for the pre-debulked and debulked situations but also exhibits the variation of the end-to-end pressure drop throughout the cycle.

Note that there is a single curve for the pressure drop without distinction between the pre-debulked and debulked situations. This is because the two situations share a common end-to-end pressure drop as the driving potential for fluid flow. This use of a common pressure drop imposed on the two artery configurations was deemed the most appropriate way of comparing their fluid flow capabilities.

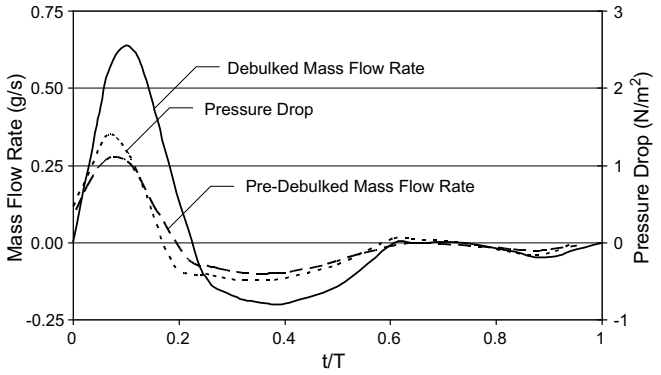

Fig. 6. Mass flowrates for pre-debulked and debulked arteries in response to a timewise cardiac pressure variation.

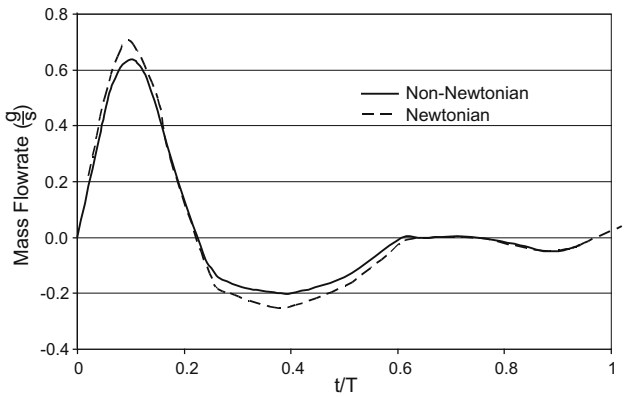

Fig. 7. Effect of non-Newtonian and Newtonian constitutive models on the mass flowrate in a debulked artery.

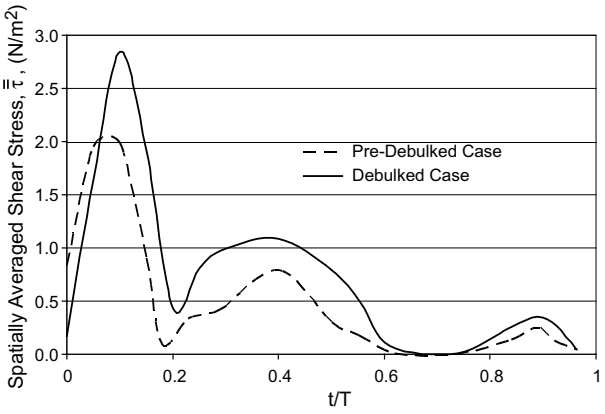

Fig. 8. Spatially averaged (circumferential and longitudinal) wall shear stress.

Of particular interest with regard to Fig. 6 is that the timewise variations of the fluid flow lag those of the pressure. For example, the pressure changes sign well before the respective flows change direction. This occurrence is in evidence both when the pressure changes from positive to negative and also when the change is from negative to positive.

Attention will now be turned to results obtained using a Newtonian constitutive equation. A comparison between the mass

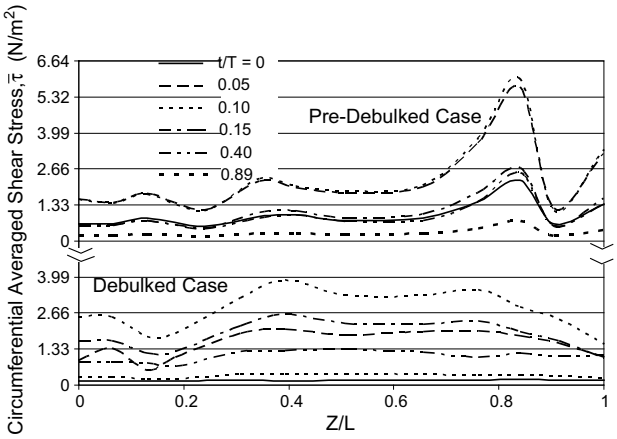

Fig. 9. Circumferentially averaged wall shear stress variations along the length of the investigated artery as a function of time.

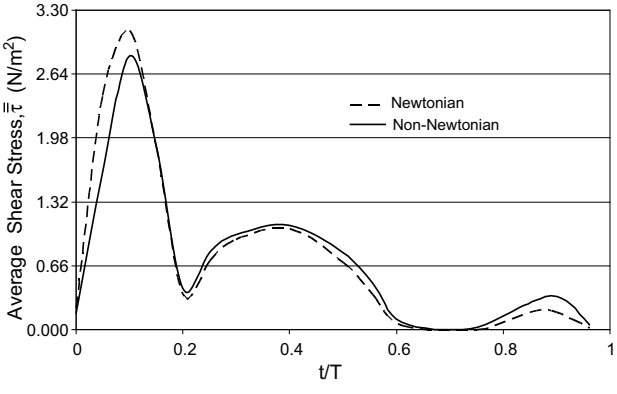

Fig. 10. Comparison of spatially averaged wall shear for Newtonian and non-Newtonian constitutive models. The results correspond to flow simulations through the debulked artery segment.

flowrate for the debulked artery calculated with the non-Newtonian and Newtonian models is made in Fig. 7. The figure shows that for both the systole and diastole periods, the predicted flowrates for the Newtonian model exceeded those for the non-Newtonian model. The deviations are moderate but consistent throughout the entire cycle. This finding can be made plausible on the basis of physical reasoning. The non-Newtonian model gives rise to an effective viscosity that is higher than the viscosity that appears in the Newtonian model. The relevance of the choice of the constitutive model will be dealt with shortly when the shear stress results are presented.

5.2. Wall shear stress results

It is well established by Ku [14] and Taylor et al. [27] that the thickness of the plaque layer is strongly related to the magnitude of the wall shear stress. This fact calls attention to the shear stress as an important factor in the development or the arrestment of a plaque layer. In particular, it is known that high shear stresses are protective with respect to the avoidance of plaque buildup.

The shear stress may be examined from several standpoints. In essence, it is a local and instantaneous quantity, depending on position (circumferential and longitudinal) and on time. A second portrayal of the shear stress might be made by first performing a circumferential average over lumen perimeter at various longitudinal positions, resulting in longitudinal–spatial and temporal variations. A global spatial average, over both circumferential and longitudinal variations, is another useful form of the shear. This double average, $\bar{\bar{\tau}}$, varies with time.

The first of the shear results to be presented is the timewise-variation of $\bar{\bar{\tau}}$, both for the undebulked and debulked artery segments. These results, presented in Fig. 8, correspond to the non-Newtonian model. In a subsequent figure, these results will be compared with those based on the Newtonian model.

An overall appraisal of this figure indicates that the magnitude of $\bar{\bar{\tau}}$ for the debulked artery segment is, for most of the cardiac cy-

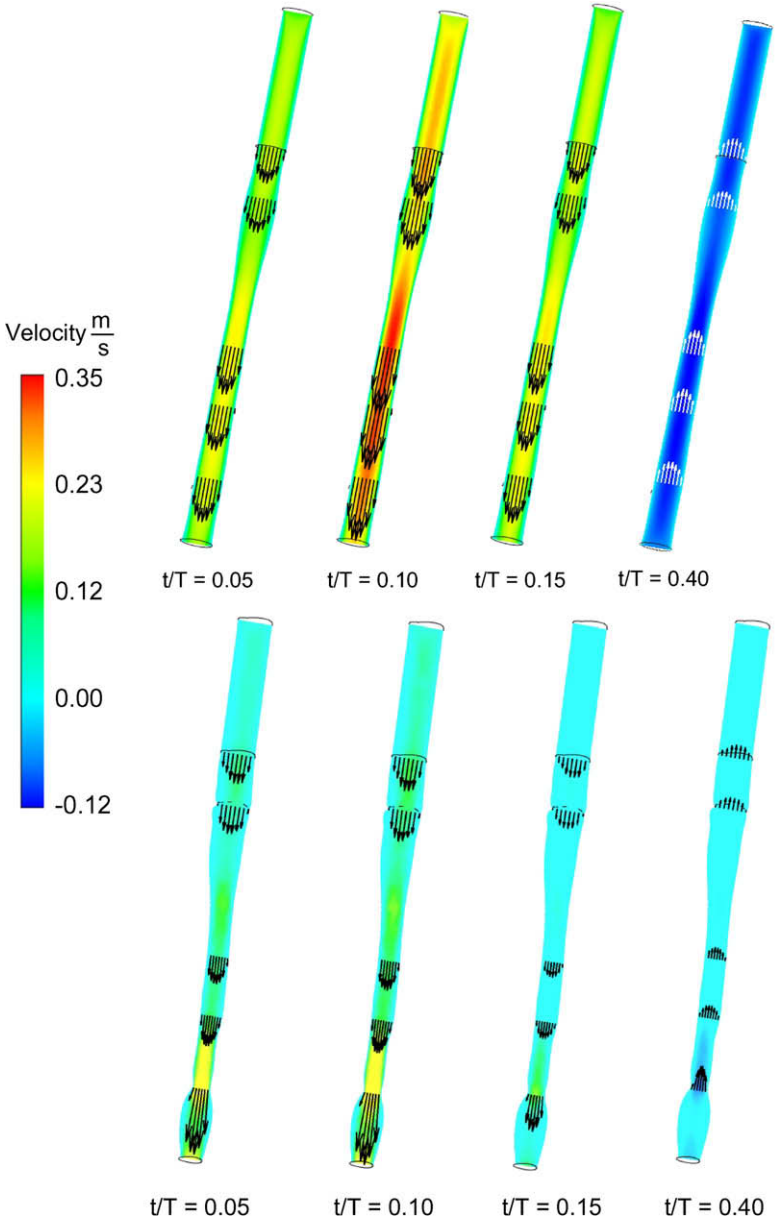

Fig. 11. Velocity vector and contour diagrams for the debulked artery segment (upper tier) and the pre-debulked segment (lower tier). The color is indicative of the magnitude of the axial velocity, while the lengths of the vectors correspond to the velocity magnitude.

cle, larger than that for the pre-debulked segment. When considering this result, it is relevant to take account of the many factors that influence the magnitude of the wall shear. Among these are the magnitude of the velocity, the roughness of the lumen wall, and larger scale geometric features. Also, in a time-dependent situation such as that considered here, the inertia of the fluid in responding to timewise pressure variations is significant with regard to the magnitude of the wall shear stress. This issue is of particular relevance at the beginning of the systolic period. As can be seen from Fig. 8, during that period, the shear stress for the pre-debulked case is higher than that for the debulked artery. It is believed that this ordering of the shear results is directly related to the lower inertia of the pre-debulked flow. Aside from this relatively short period of time, it is seen that the shear stresses for the debulked case are larger than those for the pre-debulked situation. This arrangement is clearly the result of the greater magnitude of the velocities for the former.

A more local view of the shear stress results is exhibited in Fig. 9. In that figure, the circumferential averaged shear stress, $\bar{\tau}$, is plotted as a function of position along the investigated artery segment for selected instances within a cardiac cycle. The figure is subdivided into two levels, the upper corresponding to the pre-debulked artery and the lower to the debulked case. Each of these levels has its own ordinate scale.

The main issues to be examined in Fig. 9 are the longitudinal variations of the shear stress for the respective pre-debulked and debulked cases. For the former, if the rise in the shear stress at the downstream end of the artery section is ignored, it appears that for the remainder of the section, the longitudinal variations are smaller than those for the debulked case. The aforementioned downstream rise can be understood by referring to Fig. 3a. That figure shows a necking down of the artery cross-section just before the downstream end of the segment, and it is the higher velocities that result from the diminished cross-section that are responsible for the rise in shear stress. The subsequent drop and rise of the shear stress coincide with an enlargement and follow-on contraction of the lumen.

If attention is next turned to the debulked case, the undulation of the shear stress curves in the upstream half of the artery segment can be closely keyed to the variations in the artery cross-section that are in evidence in Fig. 3b.

Focus will now be directed to a comparison between the spatially averaged wall shear stress for the cases of Newtonian and

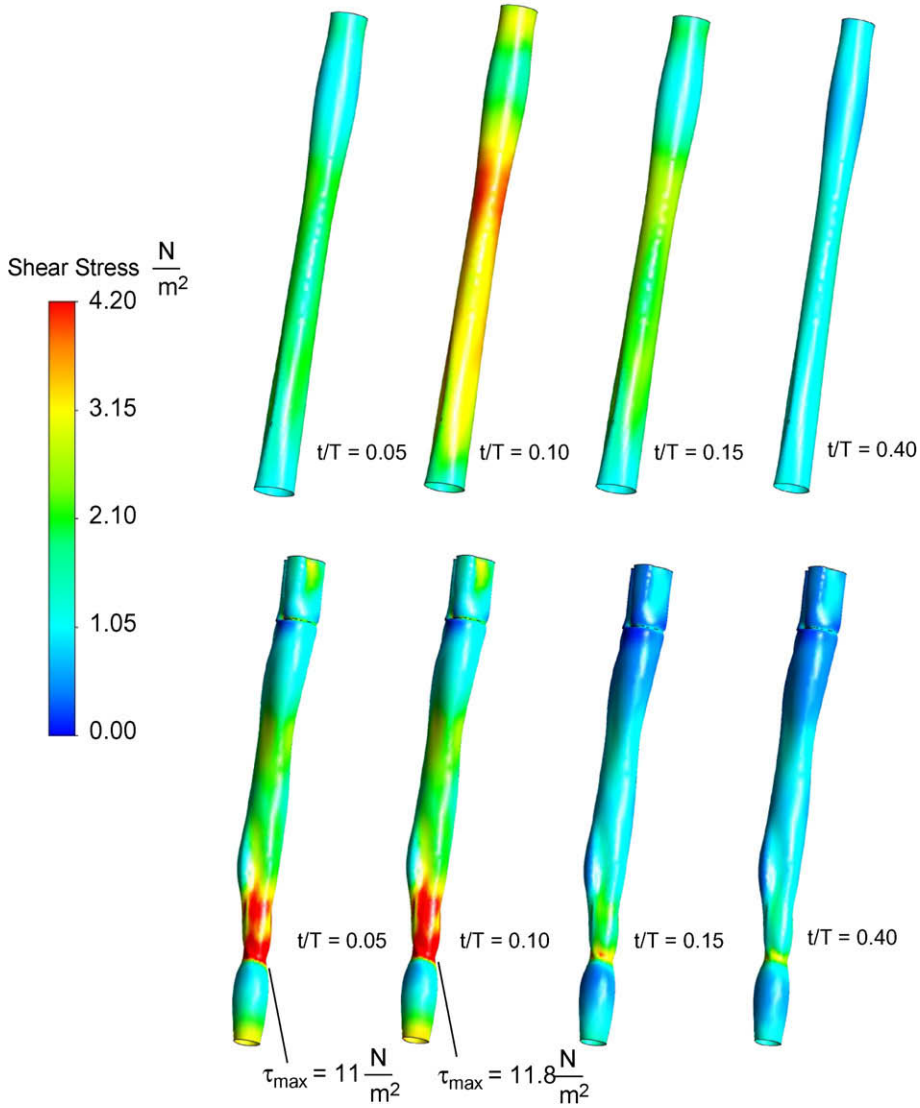

Fig. 12. Wall shear stress patterns corresponding to the debulked (upper tier) and pre-debulked (lower tier) artery segment. The magnitude of the wall shear is color-keyed to the legend at the left. For the three leftmost diagrams in each tier, the direction of the wall shear is vertically downward whereas for the rightmost diagram, the stress direction is vertically upward.

non-Newtonian flows through the debulked artery segment. This information is displayed in Fig. 10 where the averaged shear stress is plotted as a function of time throughout the cardiac cycle. In general, it is seen that the temporal variations of the shear for the two cases tend to track each other. There are, however, differences in detail. In particular, in the early part of the systolic portion, there are significant differences in the shear, with that for the Newtonian case exceeding the non-Newtonian values. A plausible explanation of this finding may be made by recognizing that at high shear rates, the Newtonian viscosity significantly exceeds the effective non-Newtonian viscosity. Furthermore, high shear rates may be associated with higher velocities. The combination of these observations supports the findings conveyed in the figure.

5.3. Global patterns of flow and wall shear stress

Focus will now be directed to exhibiting the patterns of fluid flow and wall shear stress which prevail throughout the selected artery segment. First, a set of diagrams setting forth velocity information is presented in Fig. 11. The figure is subdivided into upper and lower tiers which correspond, respectively, to the debulked and pre-debulked artery segments. In each tier, there are four contour diagrams which are parameterized by the instant of time to which they correspond. This information was extracted from the three-dimensional velocity solutions by means of a cutting plane which was passed through the largest diameter of the inlet cross-section of the arterial segment. The axial velocity magnitudes are conveyed by color while the lengths of the vectors correspond to the magnitude of the velocity. Note that the direction of the velocity vectors indicates the presence of forward flow (the leftmost three diagrams in each tier) and backflow (the right most diagram).

An overall view of Fig. 11 shows that the magnitudes of the velocity are greater for the debulked case. The velocity profiles for that case are relatively symmetric and orderly. On the other hand, for the pre-debulked case, there is clear evidence of the absence of symmetry and of a radial component at the location of the divergent area near the lower end of the artery segment.

Next, attention is turned to a display of the wall shear stress results exhibited in terms of color-contour diagrams in Fig. 12. In this figure, there are two tiers, respectively corresponding to the debulked and pre-debulked cases. When viewed in an overall manner, it is seen that the level of the shear stresses in the debulked case exceed those of the pre-debulked case. Only in very localized regions, specifically at the abrupt contraction situated just upstream of the lower end of the artery, are there large shear stresses for the latter case. The presence of these high shear stress values has already been identified in connection with the discussion of Fig. 9. In general, the shear stresses are more uniform in the debulked artery than in the pre-debulked artery.

6. Concluding remarks

It has been demonstrated that fluid mechanic analysis can play a significant role in the evaluation of medical therapeutic procedures. The particular situation that has been dealt with here is the debulking (plaque removal) from small arteries. The major issue that motivated this work is the need to evaluate the end result of the procedure. By means of a three-dimensional, unsteady fluid flow analysis in both the pre-debulked and debulked artery geometries, it was found that the debulking methodology (orbital atherectomy), accomplished by use of the Diamondback 360 Orbital Atherectomy System (Cardiovascular Systems Inc., St. Paul, MN) led to increases in blood flows on the order of 2.5 times for both the systole and diastole periods of the cardiac cycle based on the application of the timewise end-to-end pressure variation to both the pre-debulked and debulked cases.

It is recognized that the magnitude of the wall shear stresses exerted by the blood flow has a significant effect on plaque accumulation and intimal wall thickness. Consequently, special attention was given to the magnitudes of the wall shear for both the pre-debulked and debulked artery segments. It was found that, in general, the shear stresses in the debulked artery were both more uniform and higher than those in the pre-debulked artery. This favorable result suggests that the rate of plaque accumulation and arterial wall thickening in arteries will be diminished by the debulking.

Acknowledgement

Support of H. Birali Runesha and the Supercomputing Institute for Digital Simulation and Advanced Computation at the University of Minnesota is gratefully acknowledged.

References

[1] F. Abraham, M. Behr, M. Heinkenschloss, Shape optimization in steady blood flow: a numerical study of non-Newtonian effects, Comp. Methods Biomech. Biomed. Eng. 8 (2005) 127–137.
[2] T. Barth, D. Jesperson, The design and applications of upwind schemes on unstructured meshes. AIAA Paper no. 89-0366, 1989.
[3] A. Berthier, R. Bouzerar, C. Legallais, Blood flow patters in an anatomically realistic coronary vessel: influence of three different reconstruction methods, J. Biomech. 35 (2002) 1347–1356.
[4] R. Bird, W. Stewart, E. Lightfoot, Transport Phenomena, John Wiley and Sons, New York, NY, 1960.
[5] J. Chen, X. Lu, Numerical investigation of the non-Newtonian pulsatile blood flow in a bifurcation model with a non-planar branch, J. Biomech. 39 (2006) 818–832.
[6] Y. Cho, K. Kensey, Effects of the non-Newtonian viscosity of blood on flows in a diseased arterial vessel. Part 1: steady flows, Biorheology 28 (1991) 241–261.
[7] Z. Ding, K. Wang, J. Li, X. Cong, Flow field and oscillatory shear stress in a tuning-fork-shaped model of the average human carotid bifurcation, J. Biomech. 34 (2001) 1555–1562.
[8] A. Fronek, M. Coel, E. Bernstein, Quantitative ultrasonographic studies of lower extremity flow velocities in health and disease, Circulation 53 (1976) 957–960.
[9] F. Gijsen, F. van de Vosse, J. Janssen, The influence of the non-Newtonian properties of blood on the flow in large arteries: steady flow in a carotid bifurcation model, J. Biomech. 32 (1999) 601–608.
[10] M. Grigoni, C. Daniele, M. Umberto, C. Del Gaudio, G. D'Avenio, A. Balducci, V. Barbaro, A mathematical description of blood spiral flow in vessels: application to a numerical study of flow in arterial bending, J. Biomech. 38 (2005) 1375–1386.
[11] B. Hutchinson, G. Raithby, A multigrid method based on the additive correction strategy, Numer. Heat Transfer B 9 (1986) 511–537.
[12] B. Johnston, P. Johnston, S. Corney, D. Kilpatrick, Non-Newtonian blood flow in human right coronary arteries: steady state simulations, J. Biomech. 37 (2004) 709–720.
[13] U. Krueger, J. Zanow, H. Scholz, Computational fluid dynamics and vascular access, Artif. Organs 26 (2002) 571–575.
[14] D. Ku, Blood flow in arteries, Ann. Rev. Fluid Mech. 29 (1997) 399–434.
[15] J. LaDisa, I. Guler, L. Olson, D. Hetterick, J. Kersten, D. Warltier, P. Pagel, Three-dimensional computational fluid dynamics modeling of alterations in coronary wall shear stress produced by stent implantation, Ann. Biomed. Eng. 31 (2003) 972–980.
[16] Q. Long, X. Xu, K. Ramnarine, P. Hoskins, Numerical investigation of physiologically realistic pulsatile flow through stenosed arteries, J. Biomech. 34 (2001) 1229–1242.
[17] S. Majumdar, Role of underrelaxation in momentum interpolation for calculation of flow with nonstaggered grids, Numer. Heat Transfer B 13 (1988) 125–132.
[18] P. Marques, M. Oliviera, A. Franca, M. Pinotti, Modeling and simulation of pulsatile blood flow with a physiologic wave pattern, Artif. Organs 27 (2003) 478–485.
[19] I. Marshall, S. Zhao, P. Papathanasopoulou, P. Hoskins, X. Xu, MRI and CFD studies of pulsatile flow in healthy and stenosed carotid bifurcation models, J. Biomech. 37 (2004) 679–687.
[20] P. Neofytou, D. Drikakis, Non-Newtonian flow instability in a channel with a sudden expansion, J. Non-Newtonian Fluid Mech. 111 (2003) 127–150.
[21] S. O'Callaghan, M. Walsh, T. McGloughlin, Comparison of finite volume, finite element and theoretical predictions of blood flow through an idealized femoral artery, in: 2003 Summer Bioengineering Conference, June 25–29, Key Biscayne, Fl, 2003.

[22] M. Oshima, R. Torii, T. Kobayashi, N. Taniguchi, K. Takagi, Finite element simulation of blood flow in the cerebral artery, Comp. Methods Appl. Mech. Eng. 191 (2001) 661–671.
[23] C. Rhie, W. Chow, A numerical study of the turbulent flow past an isolated airfoil with trailing edge separation, AIAA Paper no. 82-0998, 1982.
[24] N. Shahcheraghi, H. Dwyer, A. Cheer, A. Barakat, T. Rutaganira, Unsteady and three-dimensional simulation of blood flow in the human aortic arch, J. Biomech. Eng. 124 (2002) 378–386.
[25] D. Tang, C. Yang, S. Kobayashi, D. Ku, Steady flow and wall compression in stenotic arteries: a three-dimensional thick-wall model with fluid–wall interactions, J. Biomech. Eng. 123 (2001) 548–557.
[26] D. Tang, C. Yang, H. Walker, S. Kobayashi, D. Ku, Simulating cyclic artery compression using a 3d unsteady model with fluid–structural interactions, Comp. Struct. 80 (2002) 1651–1665.
[27] C. Taylor, T. Hughers, C. Zarins, Finite element modeling of three-dimensional pulsatile flow in the abdominal aorta: relevance to atherosclerosis, Ann. Biomed. Eng. 26 (2000) 975–987.
[28] F. Walburn, D. Schneck, A constitutive equation for whole human blood, Biorheology 13 (1976) 201.
[29] D. Liepsch, S. Moravec, Pulsatile flow of non-Newtonian fluids in distensible models of human arteries, Biorheology 20 (1983) 745.
[30] Abraham, Sparrow, Simulation of fluid flow through a trauma fluid-warming device, Laboratory for Heat Transfer and Fluid Flow Practice, Report AZ-1, December, 2006.